Fermi Surface and Electronic Structure of Indium*

N. W. ASHCROFT AND W. E. LAWRENCE
Laboratory of Atomic and Solid State Physics, Cornell University, Ithaca, New York 14850
(Received 24 May 1968)

The available cyclotron-resonance, size-effect, and de Haas–van Alphen data in indium are compared with the geometry of the Fermi surface defined by secular equations of up to sixth order. The principal Fourier coefficients appearing in the secular equation are found from a simple form factor with a single adjustable parameter. The possible topologies of the Fermi surface are considered systematically in terms of structure plots appropriate to the points of high symmetry in the zone. It is found that a form factor consistent with transport properties, and which accurately reproduces the experimental dimensions on the β-arms, is sufficiently strong to remove all but minute, disconnected remnants of the α-type arms near the symmetry points K. Band structure, density of states, and cyclotron masses are calculated, and the electron-phonon enhancement of these and of the specific-heat mass is estimated from the final form factor.

I. INTRODUCTION

FOR polyvalent metals whose ions are small and tightly bound, the pseudopotential method for determining band structures[1–4] is, in principle, very useful. It is possible to treat the effective electron-ion interaction as a small perturbation on a pseudo-wave-function, which can be expressed in lowest order as a sum of plane waves, and thus leads within the local pseudopotential approximation to the usual secular equation for energy [see Eq. (1), below]. In the past it has been customary to construct potentials and pseudopotentials from first principles: This procedure can often lead to relatively large errors in the potential because of the efficient cancellation arising from orthogonalization terms resulting from the pseudopotential transformation. (The cancelled effective potential may contain in large measure the uncertainties involved in the individual terms comprising the self-consistent periodic potential.) In metals whose Fermi surfaces are accurately measured (as in Al, for example) a different approach is possible: The Fourier components of the pseudopotential can be regarded as parameters and their values deduced from experimental data on the detailed dimensions and shape of the Fermi surface. In addition to Al,[4] the same procedure, modified to include spin-orbit coupling, has been applied in the analysis of the Fermi surface of Pb.[5] Potential distortions to the Fermi surface *at* zone planes are of first order in the appropriate Fourier components and hence the method is ideally suited to polyvalent metals. We have, therefore, used a very similar approach here for face-centered-tetragonal (fct) indium. In Sec. II, we outline the free-electron structure of In and analyze, in terms of the Fourier components of the potential, the possible Fermi-surface topologies as predicted by structure plots for the various symmetry points in the zone. The calculations of the subsequent Fermi-surface structure and of extremal areas on the third zone by means of a simple model potential are outlined in Sec. III, and in Secs. IV and V we discuss the derived band structure, density of states, and related properties. Section V also contains some general results on the form of the lines of band contact for the fct structure.

II. SYMMETRY AND GENERAL STRUCTURE

Figure 1 shows the first Brillouin zone for fct In, whose low-temperature lattice constants are $a=4.5557$ Å, $c/a=1.0831$.[6] We note that since the symmetry is lower

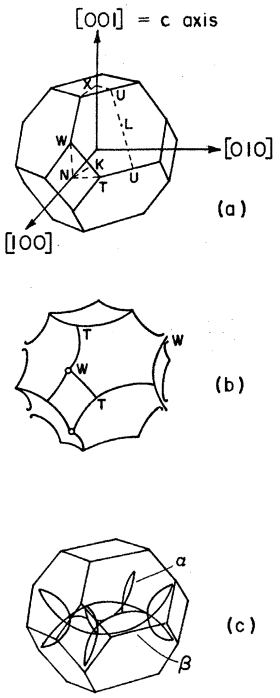

FIG. 1. (a) First Brillouin zone in fct In ($c/a=1.083$) showing the $\frac{1}{16}$ symmetry element used in setting up Eq. (1). The free-electron second-zone hole surface, multiply connected at points W, as shown in (b) and the third-zone electrons arms, multiply connected at T and pinched off at W, are also shown (c).

* Work supported in part by the U. S. Office of Naval Research under Contract No. NONR-401-(38), Technical Report No. 26, and in part by the Advanced Research Projects Agency through the Materials Science Center at Cornell University, MSC Report No. 935.

[1] W. A. Harrison, Phys. Rev. **116**, 555 (1959); **118**, 1182 (1960); **118**, 1190 (1960).

[2] M. H. Cohen and V. Heine, Phys. Rev. **122**, 1821 (1961).

[3] J. C. Phillips and L. Kleinman, Phys. Rev. **116**, 287 (1959); **116**, 880 (1959); **117**, 460 (1960).

[4] N. W. Ashcroft, Phil. Mag. **8**, 2055 (1963) (to be referred to as I).

[5] J. R. Anderson and A. V. Gold, Phys. Rev. **139**, A1459 (1965).

[6] C. S. Barett, *Advances in X-Ray Analysis* (Plenum Press, Inc., New York, 1962), p. 33.

TABLE I. Free-electron areas on the second- and third-zone surfaces in In (areas in computational units).

Zone		Plane	Area
3	β arm	(110)	0.039
	α arm	(010)	0.014
2[a]		(100)	2.83
		(00α)	2.64
		(110)	1.81
		(01α)	1.82

[a] $\pi k_F^2 = 3.79$.

than in the case for cubic fcc metals, the minimum symmetry element is now $\frac{1}{16}$ of the zone as shown in Fig. 1.

The *free-electron* Fermi surface (FS) is also shown in Fig. 1. The first zone being almost exactly filled, it consists principally of a second-zone hole surface, which is connected in the extended zone scheme at the symmetry points W. The third-zone surface consists of two sets of arms (referred to as α and β), which are multiply connected at the points T and pinched off at W. (Note that W has been used to label the point with tetrahedral symmetry.) The principal areas of interest in the free-electron model are listed in Table I. Although our discussion centers primarily on the third zone, we have given the areas on the second zone for completeness. Unless otherwise stated, we use the conventional computational units (CU) throughout, namely, $\hbar^2/2m = 2\pi/a = 1$, where m is the free-electron mass: the conversion factor for In is simply 1 CU = 7.22 eV.

There are five zone planes bounding the minimum symmetry element, and for a local pseudopotential these lead to a secular equation for energy $E_{\mathbf{k}}$ as a function of $\mathbf{k}$ as follows:

$$\begin{vmatrix} T_0(\mathbf{k},E_{\mathbf{k}}) & V_2 & V_3 & V_1 & V_1 & V_1 \\ V_2 & T_1(\mathbf{k},E_{\mathbf{k}}) & V_4 & V_1 & V_5 & V_1 \\ V_3 & V_4 & T_2(\mathbf{k},E_{\mathbf{k}}) & V_1 & V_1 & V_1 \\ V_1 & V_1 & V_1 & T_3(\mathbf{k},E_{\mathbf{k}}) & V_2 & V_3 \\ V_1 & V_5 & V_1 & V_2 & T_4(\mathbf{k},E_{\mathbf{k}}) & V_4 \\ V_1 & V_1 & V_1 & V_3 & V_4 & T_5(\mathbf{k},E_{\mathbf{k}}) \end{vmatrix} = 0, \tag{1}$$

where we abbreviate the principal Fourier components as

$$V_1 = V_{1,1,\alpha}; \quad V_2 = V_{0,0,2\alpha}; \quad V_3 = V_{2,0,0}; \quad V_4 = V_{2,0,2\alpha}; \quad V_5 = V_{1,1,3\alpha}.$$

In Eq. (1), we set $\alpha = a/c$; its diagonal terms are

$$T_0(\mathbf{k},E_{\mathbf{k}}) = \mathbf{k}^2 - E_{\mathbf{k}},$$
$$T_1(\mathbf{k},E_{\mathbf{k}}) = [\mathbf{k} - (0,0,2\alpha)]^2 - E_{\mathbf{k}},$$
$$T_2(\mathbf{k},E_{\mathbf{k}}) = [\mathbf{k} - (2,0,0)]^2 - E_{\mathbf{k}},$$
$$T_3(\mathbf{k},E_{\mathbf{k}}) = [\mathbf{k} - (1,1,\alpha)]^2 - E_{\mathbf{k}},$$
$$T_4(\mathbf{k},E_{\mathbf{k}}) = [\mathbf{k} - (1,1,\bar{\alpha})]^2 - E_{\mathbf{k}},$$
$$T_5(\mathbf{k},E_{\mathbf{k}}) = [\mathbf{k} - (1,\bar{1},\alpha)]^2 - E_{\mathbf{k}}.$$

Since the effect of higher bands on the energy levels at the symmetry points is small (as can be demonstrated readily by perturbation theory), we can discuss the level structure at K, W, T, and U in terms of smaller secular equations as outlined in Appendix A [Eqs. (A1)–(A4)].

The free-electron sphere passes just outside the symmetry point T and just inside W. The actual Fermi surface suffers considerable distortion in this region. To determine the connectivity we can, following the methods of I,[4] plot regions of occupation or nonoccupation of levels at the various symmetry points and thereby predict the topological structure of the Fermi surface that accompanies a particular set of Fourier components. To accomplish this, we require the energy levels at the symmetry points; these are easily obtained as the solutions of the secular equations (A1)–(A4).

In Figs. 2–4 we have given the structure plots appropriate to the symmetry points K, U, W, and T defined in Fig. 1. The diagrams have the following interpretation: 1 implies a single zone occupied at the given point, 2 means two zones occupied, and so on. Note that the Fermi energy used in Eqs. (A9)–(A12) is in fact appropriate to the final choice of band gaps that yield the correct areas on the β-arms. The detailed form

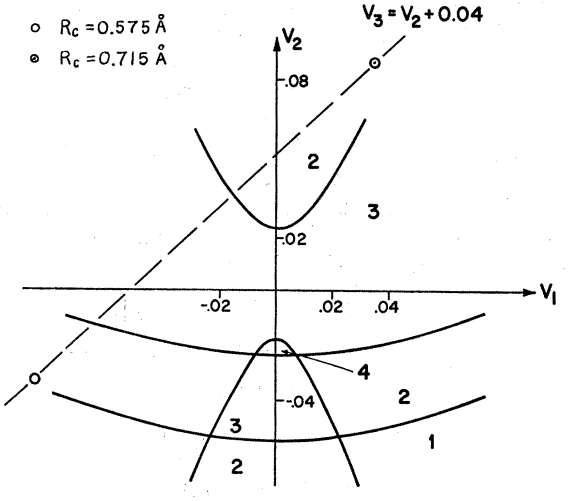

FIG. 2. Structure plot for the symmetry point T, where normally for $V_1 = V_2 = V_3 = 0$ four zones are occupied. Our plot does not show this because the dependence of the structure at T upon all three principal band gaps requires an additional constraint. We assume $V_3 - V_2 = 0.040$, which is found from Eq. (2) to be valid over a wide range of R_c.

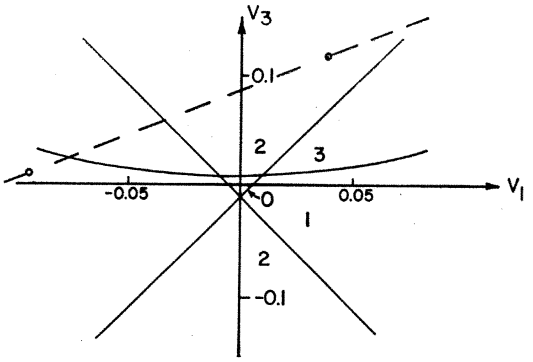

FIG. 3. Structure at W, showing no zones occupied for the free-electron bands.

of the plots is, in general, not altered when any Fermi energy close to the free-electron value is used. (The changes in E_F are second order in the V_G's as discussed below.)

The general principle involved in fitting pseudopotentials to Fermi-surface data is quite straightforward (Ref. 4). Fourier components are chosen, the Fermi energy ensuring the correct volume is calculated, and extremal areas in various zones are directly computed. The latter are compared with experimental Fermi-surface dimensions and areas, and the Fourier components are adjusted until agreement is achieved. With two independent components, as in Al,[4] the method is lengthy; with three or more, as here, the procedure can be prohibitive. However, we take note of the fact that the Fourier components V_G of the pseudopotential are in fact simply ordinates (on the complete form factor) evaluated at the reciprocal lattice points. Model-potential calculations of form factors for simple metals have been shown by Heine and Abarenkov[7] to be smooth curves (for scattering on the Fermi surface as required here). More importantly, however, the form factors exhibit nodes, and the shortest reciprocal lattice points lie quite close to the position of the first of these.

The "experimental" values of V_G for several simple metals[4,5,8] are reproduced reasonably well by model-potential calculations. It has recently been observed that the first few Fermi-surface-derived Fourier components lie on a somewhat simpler form factor, namely,

$$V(x)=-\lambda^2\cos sx/[x^2+\lambda^2 f(x)], \qquad (2)$$

where energy is measured in units $(\frac{2}{3})E_F$, x is the wave-number variable measured in units of $2k_F$, $s=2k_FR_c$, and

$$f(x)=\tfrac{1}{2}+(1-x^2/4x)\ln|(1+x)/(1-x)|\,g(x).$$

In Eq. (2), $\lambda^2=(\pi a_0 k_F)^{-1}$, and $g(x)$ is the form of exchange correction to the dielectric function as used by Heine and Abarenkov, i.e.,

$$g(x)=1-[x^2/2(x^2+\beta)].$$

The constant $\beta=\lambda^2+0.5$. For our purposes, the precise form of exchange is not too important, since the denominator of (2) is dominated by x^2 at the reciprocal lattice vectors. The single parameter R_c appearing in (2) is a measure of the range of pseudopotential cancellation in the core region. Its value is fairly close to the ionic radius.[8]

In pursuing the values of V_1, V_2, and V_3 that reproduce the data, we have assumed that all three lie on a smooth curve, and moreover, that, as with other simple metals (e.g., Al, Pb), the curve can be reproduced with sufficient accuracy by appropriate choice of R_c. The possible extremal Fermi-surface areas in In range over nearly four orders of magnitude in size. The form factor given by (2) reproduces these successfully (as it does for a range of three orders of magnitude in area in Al), and it appears that, at least for values of x around unity, the simple form factor should require only small refinements.

The band gaps V_1, V_2, and V_3 given by Eq. (2) are shown on the structure plots in Figs. 2–4. To determine the correct Fermi energy, we have used as a first approximation (as in I) the simple perturbation-theory result for the shift Δ in energy produced by a Bragg

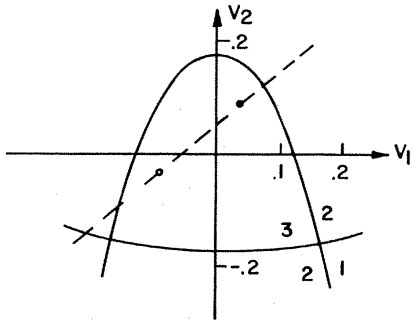

(a)

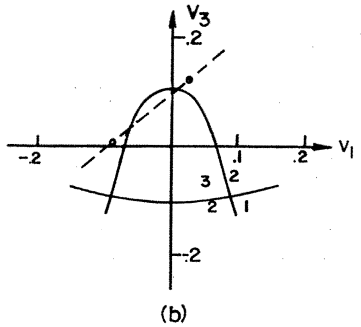

(b)

FIG. 4. We plot (a) and (b) on the same scale to contrast the structure at U, where the principal β-arm section is located, and at K, where the α-arm section would be expected.

[7] V. Heine and I. Abarenkov, Phil. Mag. **9**, 451 (1964); A. O. E. Animalu and V. Heine, Phil. Mag. **12**, 1249 (1965).

[8] N. W. Ashcroft, Phys. Letters **23**, 48 (1966); J. Phys. C **1**, 242 (1968).

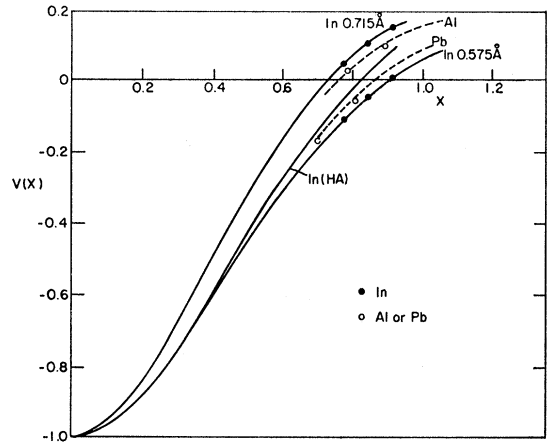

FIG. 5. Form factors for In, Al, and Pb, with the arguments $x_1=0.769$, $x_2=0.842$, $x_3=0.911$ marked for In. The Fourier coefficients for Al are taken from Ref. 1, and those for Pb are taken from Anderson and Gold (Ref. 5). The form factors that pass through these points are given by Eq. (2), with $R_c=0.59$ Å for Al and $=0.57$ Å for Pb. Energies are measured in units of $(\frac{2}{3})E_F$ and wave vectors in units of $2k_F$. The curve labelled HA is the Heine-Abarenkov model potential for In (Ref. 7).

plane with Fourier coefficient V_G:

$$\Delta_G = V_G^2/8E_F^0\, x_G \ln|(1+x_G)/(1-x_G)|\,. \qquad (3)$$

In the case of In, where we require some precision in the discussion of the α arms (see Sec. III), we have also compared the above result with machine calculations (which adjust E_F for a given set of V_G's to yield a Fermi surface enclosing 3 electrons/atom), and found that corrections to the energy shift (3) were required. In comparison to E_F^0 (1.205), we find energies for pertinent values of R_c (see below) to be

E_F	$R_c=0.575$ Å	$R_c=0.715$ Å
Perturbation theory:	1.194	1.182
Machine (volume calculations):	1.203	1.194.

III. CALCULATED PROPERTIES: COMPARISON WITH EXPERIMENT

The available experimental data fall roughly into three groups: (i) de Haas–van Alphen measurements of Brandt and Rayne[9] (ii) cyclotron mass measurements of Mina and Khaikin,[10] and (iii) size-effect measurement of Gantmakher and Krylov.[11] In this section, we focus our attention on the results of the first group and we compare experimental areas with extremal areas arising from the various topologies predicted by Figs. 2–4 [and Eqs. (A9)–(A12)]. We find that *two* choices, $R_c=0.575$ Å and $R_c=0.715$ Å, yielding form factors shown in Fig. 5, give the correct extremal cross sections for the β arm and correct Fermi-surface volumes. The band gaps corresponding to the two choices for R_c are $V_1=-0.091$, $V_2=-0.038$, $V_3=0.005$; and $V_1=0.037$, $V_2=0.087$, $V_3=0.125$, respectively, in computational units. The principal sections are shown, together with the free-electron sections, in Fig. 6. In both cases, the β-arm system has a ring structure (appropriate to topologies of Fig. 2) as shown in Fig. 7, and is thus similar to the third-zone structure in Al.[4] The areas of the necks near the corners of the rings are of order $\frac{1}{2}$ the area of the principal sections for $R_c=0.715$ Å, but $\sim 1/30$ the area for $R_c=0.575$ Å, and we attribute (as do Mina and Khaikin) the small cyclotron masses to these regions (see Table III). Only for $R_c=0.575$ Å do any remnants of the α arms remain—the other model removes them completely. These minute arms (or "platelets") are shown on Figs. 6 and 7 with their β-arm counterparts. Corresponding principal areas [in the (011) plane] are 4% of the principal area of the β arm, 10^{-3} CU, and the volume of each remnant α arm is

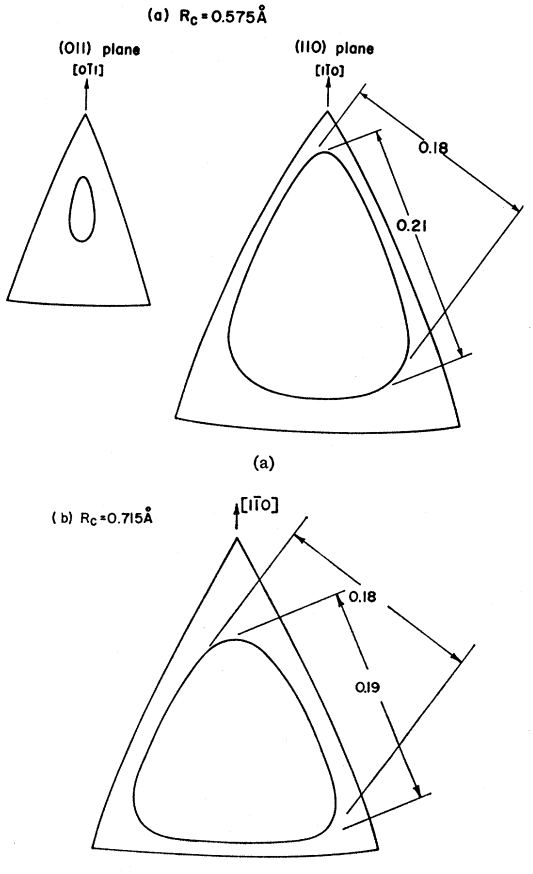

FIG. 6. Free and perturbed β-arm principal (110) section at U. We have marked in dimensions corresponding to measurements of Gantmacher and Krylov, who obtain 0.22 and 0.18. Also shown is the principal section of the α-arm remnant with $R_c=0.575$ Å, which appears in the (011) plane near K.

[9] G. B. Brandt and J. A. Rayne, Phys. Letters **12**, 87 (1964); Phys. Rev. **132**, 1512 (1963).

[10] R. T. Mina and M. S. Khaikin, Zh. Eksperim. i Teor. Fiz. **51**, 62 (1966) [English transl.: Soviet Phys.—JETP **24**, 42 (1966)].

[11] V. F. Gantmakher and I. P. Krylov, Zh. Eksperim. i Teor. Fiz. **49**, 1054 (1965) [English transl.: Soviet Phys.—JETP **22**, 734 (1966)].

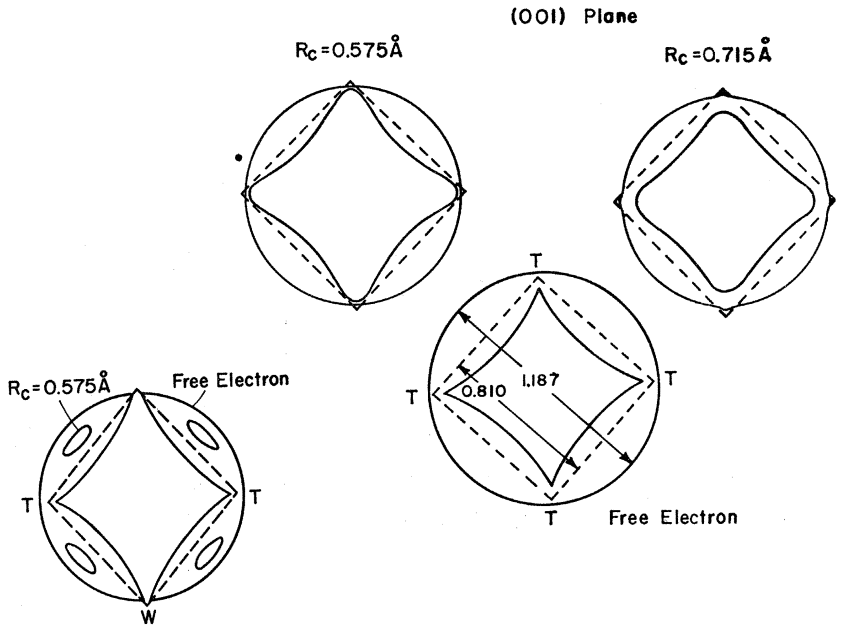

FIG. 7. Free and perturbed sections of the β arm in the (001) plane, with ring structure preserved in both models. Corresponding sections of the α arms appear in the (100) plane.

$\sim 10^{-4}$ CU. We can give the following arguments to show that if the α arms exist at all, they *must* be very small.

First, without appealing to the details of the form factor, we remark that the free-electron levels at K and U are triply degenerate, and any (small) perturbation will therefore increase the third-zone energy in the vicinity of these points, thereby reducing the size of the α (and β) arms. The slight decrease in E_F due to the presence of Bragg planes will further reduce their size. Note that $(E_F-E_U)>2(E_F-E_K)$, corresponding to a "free-electron" area for the α arm about $\frac{1}{3}$ that of the β-arm, hence the effects are proportionately more pronounced on the α-arm system.

Next, we point out that two form factors that produce the correct β-arm area and Fermi-surface volume may give different results for the α arm, because it is predominantly V_1 and V_3 that perturb the levels at K, and V_1 and V_2 the levels at U. A rough rule of thumb which serves as a criterion for the existence of α-arms is $|V_3/V_2|\lesssim\frac{1}{3}$, which occurs in our model only for R_c between 0.55 Å and 0.58 Å. As long as the band gaps lie on a smooth curve, a reasonable upper limit to the area of the α arms near K is, conservatively, $\frac{1}{10}A_\beta$. We are ruling out the unlikely possibility that V_2 could be large with V_1 and V_3 small—the only circumstance under which the α arms could be substantial.

At the zone corner points W and T, the effect of the perturbation is more complicated. As noted in Sec. I, certain combinations of band gaps can lead to multiple connectivity of the second-zone hole surface around the corners of the zone. We find markedly similar behavior to occur here. In fact, for the sets of values of V_1, V_2, and V_3, which reproduce the correct β-arm structure, the second-zone hole surface is connected by small tubes near the corners of the rhombohedral faces, as depicted in Figs. 8 and 9 (in contrast to the situation in Al, whose second-zone surface is closed). The structure at the square face is similar to that found in Al, namely, in the absence of spin-orbit coupling the second-zone hole surface is connected at single points to the (third-zone) β-arm ring. As might be expected, the details of the Fermi-surface structure near W and T are considerably different for the two model pseudopotentials. To illustrate, we list extremal areas for the second-zone junction tubes and neck regions of the β-arm system in Table II, together with the larger extremal areas observed on the third zone. The smaller sections are depicted in Figs. 10 and 11. In their earlier work,[9] Brandt and Rayne observe low-frequency oscillations corresponding to an extremal area 0.0006 CU, and with an orientational dependence very similar to that arising from the bulbous neck region of the β-arm system as given in the $R_c=0.575$ Å model (shown also in Fig. 10). This agreement is quite striking, inasmuch as a change in energy over this region of 0.2% E_F would cause these areas to change by about 50%. We should not, in fact, expect such agreement from a model as simple as ours, and cannot expect to retain it when definitive data on the α arms and the structure at W become available. Notice that the Fermi-surface dimensions around W are also very small, and experimental data on this region should give an interesting guide to refinements for the pseudopotential.

IV. EFFECTIVE MASSES AND DENSITY OF STATES

The observed resonances in the Azbel-Kaner effect in In give a measure of the differential area on the

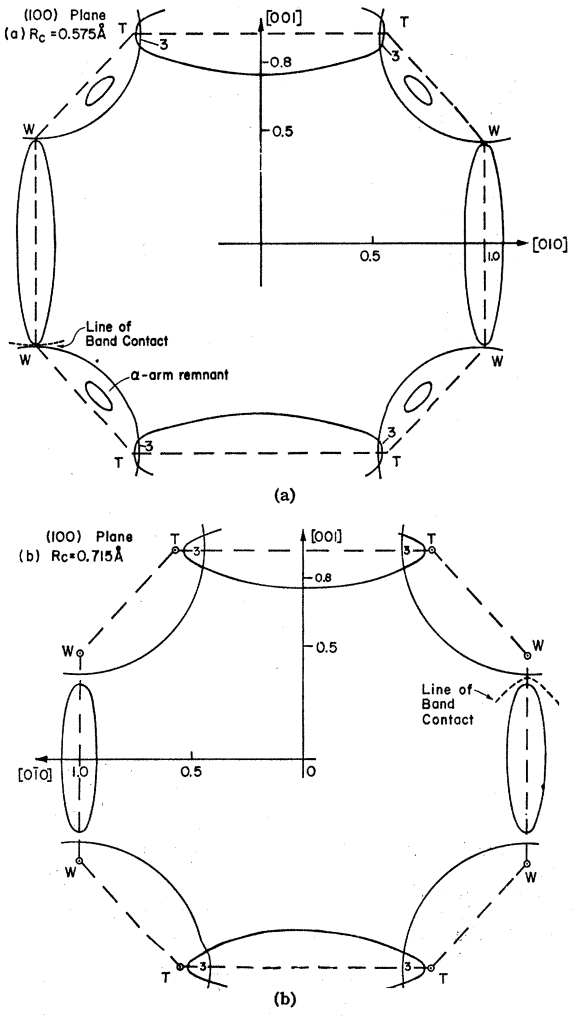

FIG. 8. (100) section of second-zone hole surface showing connecting tubes near W and β-arm necks near T, connected at single points to the hole surface. Third-zone regions are indicated by the numeral 3.

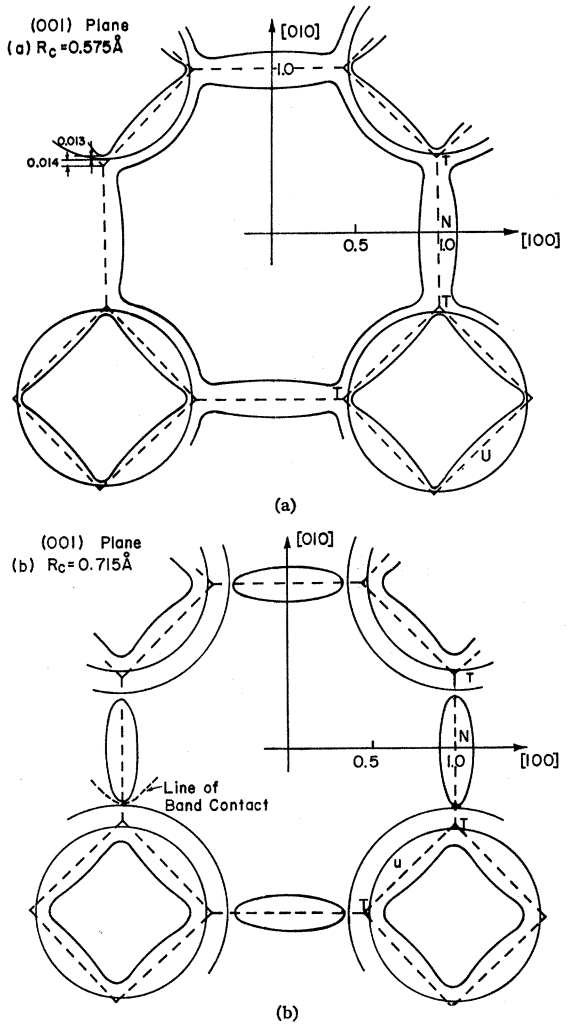

FIG. 9. (001) section of hole surface showing connecting tubes near T with the R_c=0.715 Å model.

Fermi surface in various zones. Normally the latter are expressed as cyclotron effective masses m_c^* and are given by

$$\frac{m_c^*}{m}=\frac{1}{\pi}\frac{dA}{d\epsilon}\bigg|_{\epsilon_F},$$

where A is an extremal area on the Fermi surface. The energy ϵ here is the ϵ appearing in the energy-versus-wave-number relation appropriate to the *true* band structure. It is not the energy E appearing in the secular equations used here. In Eqs. (1) and (A1)–(A4), ϵ_k is related to E_k in the (G,G) diagonal element by

$$\epsilon_k=E_k+\langle \mathbf{k}-\mathbf{G}|V_{ps}|\mathbf{k}-\mathbf{G}\rangle, \qquad (4)$$

where we have explicitly displayed the fact that the potential is a pseudopotential whose most general form is $V_{ps}=V+\hat{P}_cO$, with O being any linear operator (satisfying the translation of the lattice) and $\hat{P}_c$ being a projection operator onto the entire core space. If O is chosen to be $-V$, then $V_{ps}=V-\hat{P}_cV$ is the Austin[12] form of the potential which, by assuming $\hat{P}_c$ leads to

TABLE II. Extremal areas (in computational units) on the third-zone β-arm system and second-zone connecting tubes.

Large third-zone orbits field direction	Expt.[a]	R_c=0.715 Å	R_c=0.575 Å
[110]	0.023	0.023	0.023
[100]	0.031	0.032	0.031
[011]	0.041	0.042	0.042
Small orbits			
β neck near T[b]	0.0006	0.0093	0.0007
Second-zone tube near T[c]	···	0.0012	···
Second-zone tube near W[c]	···	0.0040	0.0003
Second-zone tube near W[d]	0.0007	···	0.0005

[a] Brandt and Rayne, Ref. 9.
[b] See Fig. 10.
[c] Extremal areas are given for field in the [100] direction.
[d] Field in the [110] direction.

[12] B. J. Austin, V. Heine, and L. J. Sham, Phys. Rev. **127**, 276 (1962).

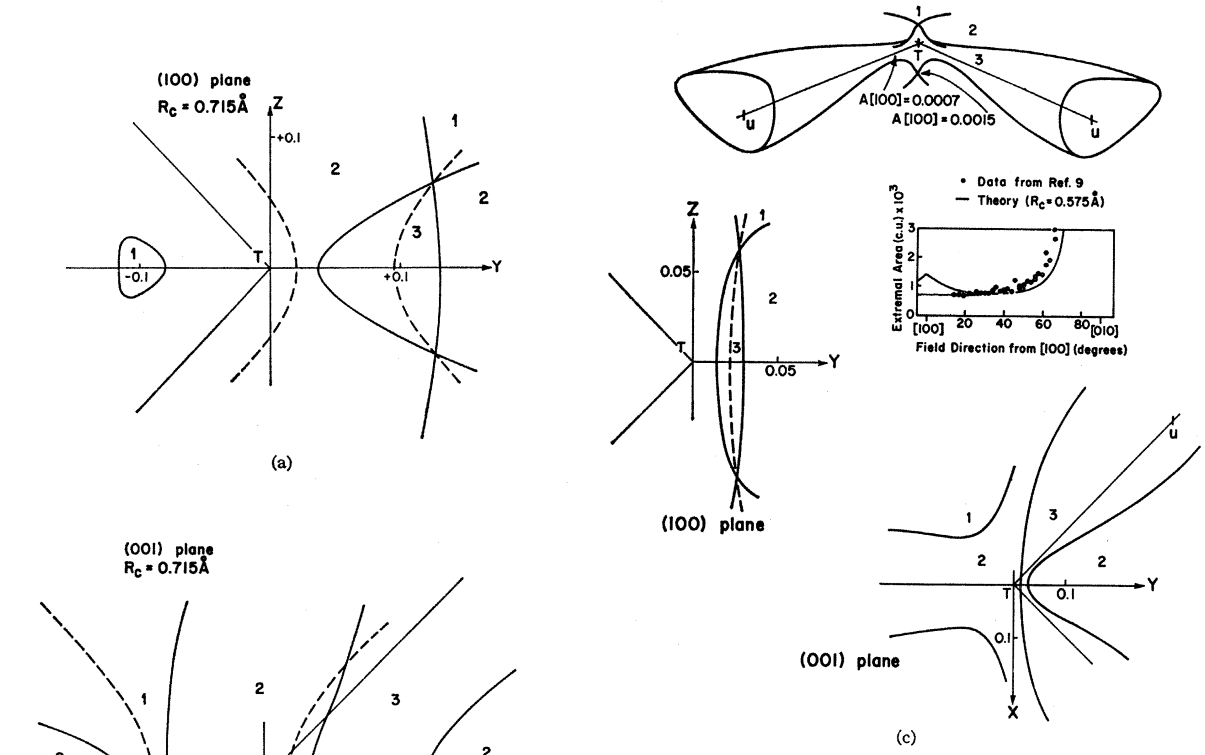

FIG. 10. Various sections of the Fermi surface near T, with the number of occupied zones in each region indicated and lines of band contact drawn in where they aid understanding of the second- and third-zone structures. The pronounced bulb on the neck of the $R_c = 0.575$ Å β arm as shown in (c) [which causes the cross-sectional area in the (100) plane to change by a factor of 2] is not present in the other model, shown in (a) and (b). The bulb makes possible the unusual angular dependence, which corresponds to the data of Brandt and Rayne. Notice the two sets of extremal areas: The larger areas represent orbits centered at T. There is also a marked qualitative difference between the second-zone surface near T. This is possible because the band contact line passing through the rhombohedral face of the zone near T represents degenerate second and third levels for $R_c = 0.715$ Å, but not for $R_c = 0.575$ Å.

essentially complete cancellation between terms for $r < R_c$, is being approximated in local form by Eq. (2). The matrix elements of V_{ps} in general depend, however, on both the energy and wave vectors of the pseudo-wave-functions. For Fermi-surface areas and their derivatives, we need to pay particular attention to the definition of the energy scale for the secular equation, in which we set

$$E_{\mathbf{k}} = \epsilon_{\mathbf{k}} - \langle \mathbf{k}-\mathbf{G} | V_{ps} | \mathbf{k}-\mathbf{G} \rangle = \epsilon_{\mathbf{k}} - V_{000}(E)$$

(as in the local pseudopotential approximation). As regards band-structure contributions to effective masses, we must, therefore, modify any derivatives taken with the secular-equation energy E by a factor

$$1 + [dV_{000}(E)/dE].$$

Thus, for example,

$$\frac{m_c^*}{m} = \frac{1}{\pi}\left(\frac{dA}{dE}\right)\left(\frac{dE}{d\epsilon}\right) = \frac{1}{\pi}\left(\frac{dA}{dE}\right)\left[1 + \frac{dV_{000}}{dE}\right]^{-1}, \quad (5)$$

and so the cyclotron masses computed by area changes defined by the secular equations used here must be corrected by a factor of

$$F_1 = \left(1 + \frac{dV_{000}(E)}{dE}\bigg|_{E_F}\right)^{-1}.$$

It is clear that this result is applicable to *all* zones. The density of states calculated by evaluating the volume shift in $\mathbf{k}$ space of the Fermi surface must also be altered in a similar way to get the true density of states. In terms of the model potential leading to (2) we incorporate the energy dependence solely in terms of $R_c(E)$. In forming $\langle V(r) \rangle$, the long-range part of the potential is cancelled off by the Coulomb field of the electron gas leaving, simply, as the energy-dependent part,

$$\langle V(r, E_F) \rangle = 4\pi n_e e^2 (R_c^2/2) = (E_F/3)\lambda^2 s^2,$$

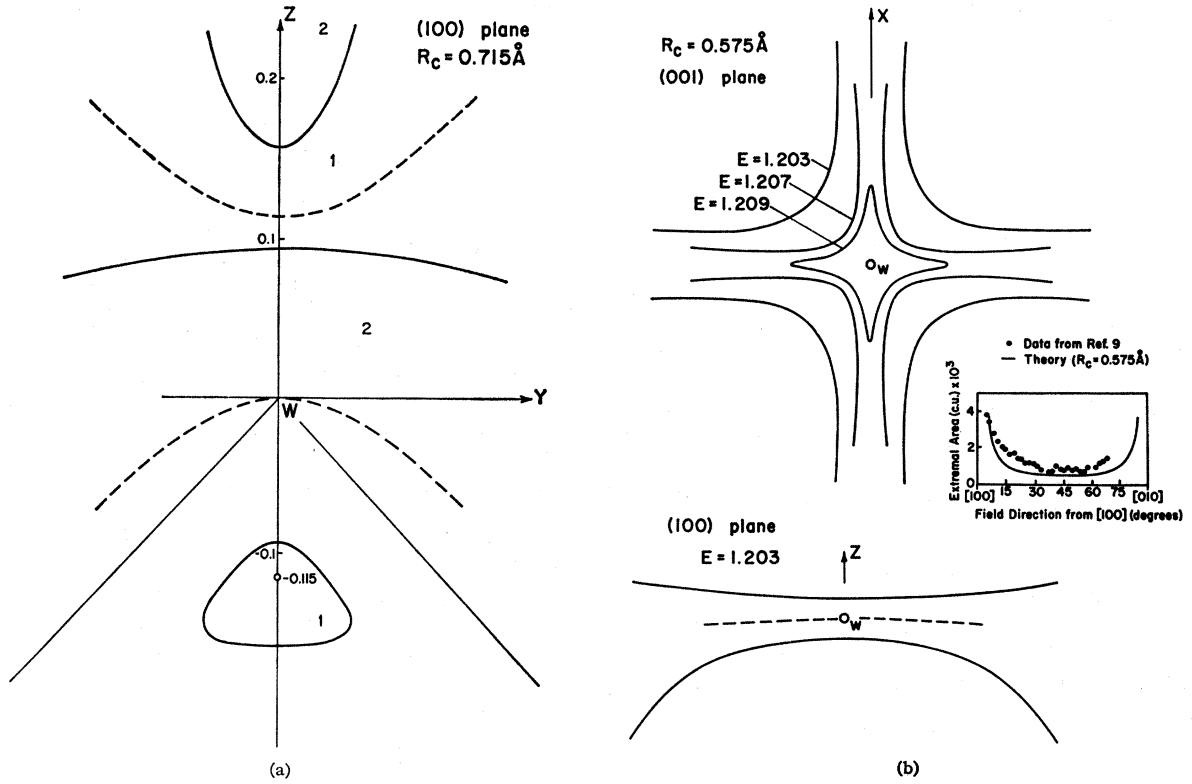

FIG. 11. Sections of the Fermi surface near W in the (100) and (001) planes. Tetrahedral symmetry permits one to view the (010) sections by inverting the (100) figures. The R_c=0.715 Å sections are depicted in (a), and in (b) are shown the *intersecting* tubes which appear with R_c=0.575 Å. The latter make possible an areal minimum in the [110] direction, A[110]=0.0005 CU, which corresponds as shown to the data of Brandt and Rayne. Our R_c=0.575 Å model gives another set of oscillations, arising from orbits centered away from W, with areal minima in the [100] and [010] directions, A[100]=0.0003 CU, as listed in Table II. Notice that a small increase in E_F replaces the tubes by pockets of electrons in the third zone.

where n_e is the electron density. It follows that

$$\left.\frac{dV_{000}}{dE}\right|_{E_F}=(\tfrac{2}{3})\lambda^2 s^2\eta,$$

where

$$\eta=\left.\frac{d\ln R_c}{d\ln E}\right|_{E_F}$$

is the parameter which expresses the energy dependence of the potential and thus leads to a determination of $A(E)$.

In addition to the energy dependence of the diagonal elements of V_{ps}, we also expect the off-diagonal elements (here, $V_{1,1,\alpha}$, $V_{0,0,2\alpha}$, and $V_{2,0,0}$) to be dependent on the energy of the valence state. We are assuming effects of nonlocality to be small, which is a reasonable approximation for scattering on the Fermi surface.[7] The energy dependence of the V_G's has an effect on the cyclotron masses, but now the shifts depend very much on the orbit concerned. To illustrate, we may write, symbolically,

$$\frac{dA}{dE}=\left(\frac{\partial A}{\partial E}\right)_V+\left(\frac{\partial A}{\partial V}\right)_E\left(\frac{dV}{dE}\right), \tag{6}$$

where the first term evaluates the differential area keeping the band gaps fixed, and the second term incorporates changes in the pseudopotential with valence energy. In terms of the parameter defined above we may rewrite Eq. (6) as

$$\left(\frac{dA}{dE}\right)=\left(\frac{\partial A}{\partial E}\right)_{R_c}+\pi\left(\frac{R_c}{A_0}\cdot\frac{\partial A}{\partial R_c}\right)\eta=\left(\frac{dA}{dE}\right)_{R_c}F_2,$$

where

$$F_2=1+\pi\left(\frac{A}{A_0}\right)\left(\frac{\partial\ln A}{\partial\ln R_c}\right)\eta\Big/\left(\frac{\partial A}{\partial E}\right)_{R_c},$$

and $A_0=\pi k_F^2$. It is now apparent that the magnitude of this term will depend sensitively on the orbit size. For a large free-electron-like orbit, as in the second zone, the effect of potential distortion on the area is, in the first place, small. As a consequence, the effects of *changes* in the potential are negligible. On the other hand, for the small third-zone orbits, potential distortion gives a large initial fractional change in the area, and changes in the potential itself and their effect on the areas cannot be neglected. Collecting the factors

together, we now find

$$\left(\frac{m_c^*}{m}\right)_{\mathrm{BS}}=\frac{1}{\pi}\left(\frac{\partial A}{\partial E}\right)_{R_c}\Bigg|_{E_F} F_1F_2.$$

To make a comparison with experiment, we must incorporate two further corrections. The first is a many-body correction to the mass due to electron-electron interactions. At electron densities appropriate here ($r_s=2.39$), Rice[13] has shown these to have a negligible effect on the over-all effective mass of a free-electron-like metal, and we expect them to be similarly small here. The other correction, due to electron-phonon coupling, is, however, not small. By way of example, Ashcroft and Wilkins[14] have shown that a state $\mathbf{k}$ at the Fermi surface leads to a contribution $\lambda_{\mathbf{k}}$ to the linear term in the total low-temperature specific heat C, of the form

$$\lambda_{\mathbf{k}}=N_{\mathrm{BS}}(E_F)\left(\frac{1}{S}\right)\int_{\mathrm{F.S.}}\frac{dS_{\mathbf{p}}}{4\pi}\frac{|g_{\mathbf{k}-\mathbf{p}}|^2}{\hbar\omega_{\mathbf{k}-\mathbf{p}}}, \tag{7}$$

so that averaging over all states $\mathbf{k}$ at the Fermi level, the linear term becomes

$$C=\gamma_0(1+\lambda)T,$$

where

$$\lambda=N_{\mathrm{BS}}\left(\frac{1}{S^2}\right)\int\frac{dS_{\mathbf{k}}}{4\pi}\int\frac{dS_{\mathbf{p}}}{4\pi}\frac{|g_{\mathbf{k}-\mathbf{p}}|^2}{\hbar\omega_{\mathbf{k}-\mathbf{p}}},$$

with $g_{\mathbf{k}-\mathbf{p}}$ the matrix element for scattering phonons of frequencies $\omega_{\mathbf{k}-\mathbf{p}}$ (S here is the actual Fermi-surface area, and for the sake of clarity we have omitted the usual sum over polarizations). In (7), $N_{\mathrm{BS}}(E_F)$ is the band-structure density of states. Turning again to the case of the cyclotron effective mass, we find that it too suffers an enhancement, although the average involved is somewhat different, being an average of the contributions of the states $\mathbf{k}$ around the extremal areas concerned and *not* over the whole Fermi surface, (as in the specific-heat case). We are therefore led to consider expressions of the form

$$\lambda_\Gamma=N_{\mathrm{BS}}(E_F)\frac{1}{l_\Gamma}\oint_{\mathrm{orbit}\ \Gamma}dk\int\frac{dS_{\mathbf{p}}}{4\pi}\frac{|g_{\mathbf{k}-\mathbf{p}}|^2}{\hbar\omega_{\mathbf{k}-\mathbf{p}}}, \tag{8}$$

where l_Γ is the path length of the extremal orbit Γ. For spherical Fermi surfaces contained within a single zone, (7) and (8) reduce to the same enhancement factor, but for distorted multiply-connected surfaces we must expect the averages to be dependent, in general, on the orbit concerned.[15] Hence, we may write, finally,

$$\left(\frac{m_c^*}{m}\right)_\Gamma=\left(\frac{m^*}{m}\right)_{\mathrm{BS}}(1+\lambda_\Gamma)$$
$$=\frac{1}{\pi}\left(\frac{dA_\Gamma}{dE}\right)_{R_c}\Bigg|_{E_F}F_1F_2(1+\lambda_\Gamma). \tag{9}$$

The calculations of F_1 and F_2 both involve a determination of η. In addition, the precise evaluation of λ_Γ requires a knowledge of the lattice spectra and these are not presently available. Although detailed estimates of the corrections cannot therefore be made, we can make reasonable calculations of the expected enhancements as follows. First, we note that the tetrahedral structure of In is not too far removed from cubic. Second, we may take the phonon dispersions on In to be similar to those in a cubic metal but scaled by an average ratio of the longitudinal and transverse sound velocities. It follows that if we can find a cubic metal (CM) whose form factor $V(x)$ in reduced units (i.e., wave vectors in units of $2k_F$ and energies in terms of $\frac{2}{3}E_F$) is similar, then

$$\frac{\lambda^{\mathrm{In}}}{\lambda^{\mathrm{CM}}}=\left(\frac{E_F{}^{\mathrm{In}}}{E_F{}^{\mathrm{CM}}}\right)^2\left(\frac{C^{\mathrm{CM}}}{C^{\mathrm{In}}}\right)\left(\frac{M^{\mathrm{CM}}}{M^{\mathrm{In}}}\right)\frac{(m_{\mathrm{BS}}{}^*)^{\mathrm{In}}}{(m_{\mathrm{BS}}{}^*)^{\mathrm{CM}}},$$

which follows directly from (7). Here, C's are sound velocities and M's are ionic masses. By assumption, the integrals in reduced units are approximately equal, and hence cancel in the expression above. The reference metal should also be trivalent and its phonon enhancement should be known, and this obviously limits us to Al whose form factor is not as close to that of In as we would like. Nevertheless, we obtain $\lambda^{\mathrm{In}}=0.60$, giving a predicted phonon-enhancement factor of 1.60, to be applied to our band-structure density of states and cyclotron effective masses. When applied to our band-structure density of states $N_{\mathrm{BS}}(E_F)/N_0(E_F{}^0)=0.91$ (to be discussed in Sec. V), we get a value of 1.45, which agrees rather too well with the experimental thermal mass,[16] $m_T{}^*/m=1.46$, taken from the coefficient of the linear term in the specific heat. The error here is probably large, but we also get good agreement with the observed cyclotron masses on the second zone, as shown in Tables III and IV. The third-zone ratios, $m_c{}^*(\mathrm{expt})/m_c{}^*(\mathrm{BS})$, are systematically greater than 1.6, however. This stems in part from variation of the enhancement factor λ_Γ discussed above. For most points on the second zone, the matrix elements $g_{\mathbf{k}-\mathbf{p}}$ referred to earlier are constructed from essentially single orthogonalized-plane-wave (OPW) wave functions; hence, as mentioned previously the orbital averages (8) would give essentially the same result as the surface average (7). How-

[13] T. M. Rice, Ann. Phys. (N. Y.) **31**, 100 (1965).
[14] N. W. Ashcroft and J. W. Wilkins, Phys. Letters **14**, 285 (1965).
[15] The ratios of $m_{\mathrm{CR}}{}^*(\mathrm{expt})/m_{\mathrm{BS}}{}^*(\mathrm{theor})$ which give $(1+\lambda)$ have shown some anisotropy in, for example, both Al and Pb (see Refs. 4 and 5).
[16] J. R. Clement and E. H. Quinnel, Phys. Rev. **92**, 258 (1953).

TABLE III. Comparison of experimental and theoretical specific-heat and cyclotron effective masses, without energy dependence of the pseudopotential included.[a]

Zone	Field direction	m_c*(expt)	R_c=0.575 Å m_c*(B.S.)	expt/th.	0.715 Å m_c*(B.S.)	expt/th.
	[110]	1.17	0.778	1.51	0.768	1.53
2	[011]	1.34	0.885	1.52	0.909	1.48
	[111]	1.54	1.022	1.51	0.970	1.59
	[110]	0.19[b]	0.113	1.68	0.110	1.60
3	[110]	0.202	0.113	1.78	0.119	1.70
near U	[100]	0.27	0.146	1.85	0.162	1.67
	[111]	0.35	0.211	1.66		
near T	[110]	0.096 (extrapolated)	0.044	2.2	0.10	0.096
Specific-heat mass		1.46[c]	0.91	1.60	0.91	1.60

[a] Values taken from Ref. 10, unless otherwise stated.
[b] Reference 9.
[c] Reference 16.

TABLE IV. Comparison of the effective masses in In with those of some other simple metals.[a]

		Na	Al	In(R_c=0.575 Å)	Pb
(m^*/m)BS		1.00	1.06	0.91	0.90
$(\delta m^*/m)$el-el		0.06	−0.01	∼0.0	0.00
$(\delta m^*/m)$el-ph		0.18	0.49	0.60	1.05
$1+(\delta m/m)$el-el$+(\delta m/m)$el-ph		1.24	1.48	1.60	2.05
	Specific-heat mass	1.25	1.37	1.60	2.20
$\left(\frac{m^*(\text{Exp.})}{m^*(\text{B.S.})}\right)$	Cyclotron mass (second zone)			∼1.50	∼2.00
	(third zone)			1.75±0.10	2.25±0.15

[a] Values other than those for In are taken from Ref. 14.

ever, this is not true for third-zone orbits, since most of their points lie close enough to Bragg planes that two or three OPW's are mixed with considerable weight. To estimate the effect of this, we perform a rough calculation (as outlined in Appendix C) of the quantity $(\lambda_{III}-\lambda_{II})$, where λ_{III} is the enhancement factor for the principal orbit of the β-arm system at U, and λ_{II} is the second-zone factor, 1.6. We choose the principal orbit of the β arm because of all third-zone orbits it is "least distorted" from the free-electron orbit, and $(\lambda_{III}-\lambda_{II})$ will probably be greater for all other third-zone orbits. We conclude that for $R_c=0.575$ Å $(\lambda_{III}-\lambda_{II})/\lambda_{II} \approx 0.15\pm0.05$, which is not large enough to account for the observed difference between second- and third-zone mass enhancements but does have the correct sign. With $R_c=0.715$ Å, $(\lambda_{III}-\lambda_{II})$ is negative.

Notice that the orbit-dependent effective-mass enhancements found here have also been observed by Gordon and Larson[17] in Al. The enhancements for the equivalent neck masses in Al are about 15% higher than the enhancement for the principal third-zone orbits. This is also the case here, although there is also some anisotropy in the enhancements: Inspection of the elastic constants in indium indicates a marked variation in the transverse and longitudinal sound velocities for the various crystallographic directions. The latter will manifest itself in the orbit averages involved in the mass enhancements, and the observed irregularities in m^*/m_{BS}^* are, as a consequence, related both to the orientation *and* orbit size.

The over-all agreement between experimental and theoretical effective masses (including electron-phonon corrections) suggests that F_1F_2 may be close to unity, i.e., η small. If we were to choose η in such a way that F_2, the orbit-dependent correction factor, brought the second- and third-zone masses into agreement (i.e., "apparent" value of λ, the same for both zones), then F_1 would differ enough from unity to destroy the *over-all* agreement existing with η small. An independent determination of η is afforded, in principle, by pressure dependence of the de Haas–van Alphen effect. However, this pressure dependence depends upon the quantity $\eta'=[(\partial \ln R_c/\partial \ln E)-1.164(\partial \ln R_c/\partial \ln a)]$ and not upon η alone, and it is difficult to separate the two dependences without explicitly constructing the pseudopotential from the core states. We have computed values of the quantity $d\ln A/dP$, as outlined in Appendix D, for comparison with the measured values of O'Sullivan *et al.*[18] In the cases of the second-zone orbits, agreement is to within about 20%. Since second-zone areal derivatives are quite insensitive to η', an unreasonably large energy dependence would be required to achieve perfect agreement for these. The third-zone areal derivative is most sensitive to η', and for $R_c=0.575$ Å, a value of $\eta'=-0.18$ gives the best fit. We have also attempted to deduce the energy dependence of our pseudopotential using the OPW-calculated energy levels of Gaspari and Das.[19] We find that $dV_{000}(E)/dE \approx 0.07$ is consistent with many of their points. This would suggest that $\eta \approx 0.11$. However, the apparent energy dependence of the $V_G(E)$ does not correspond to this value, and cannot, in fact, be represented by a single parameter of this type. Moreover, although the band structure calculated by Gaspari and Das is qualitatively similar to the curves in Fig. 12, the details are sufficiently different to remove the over-all agreement with the de Haas–van Alphen areas which are highly sensitive to the band gaps.

V. BAND STRUCTURE AND DENSITY OF STATES

We have used Eq. (1) and the values of V_1, V_2, V_3 corresponding to both values of R_c to obtain the energy dispersions of the electrons, $E(\mathbf{k})$, as a function of $\mathbf{k}$ for $\mathbf{k}$ along the various symmetry directions. These are shown in Fig. 12; we have also marked in the Fermi energy E_F as shown (see, also, Sec. VI). None of the curves in these figures includes the factor F_1, which can easily be incorporated for any possible application.

[17] W. L. Gordon and C. O. Larson, Phys. Letters **15**, 121 (1965); C. O. Larson and W. L. Gordon, Phys. Rev. **156**, 703 (1967).

[18] W. J. O'Sullivan, J. E. Schirber, and J. R. Anderson, Solid State Commun. **5**, 525 (1967).

[19] G. D. Gaspari and T. P. Das, Phys. Rev. **167**, 660 (1968).

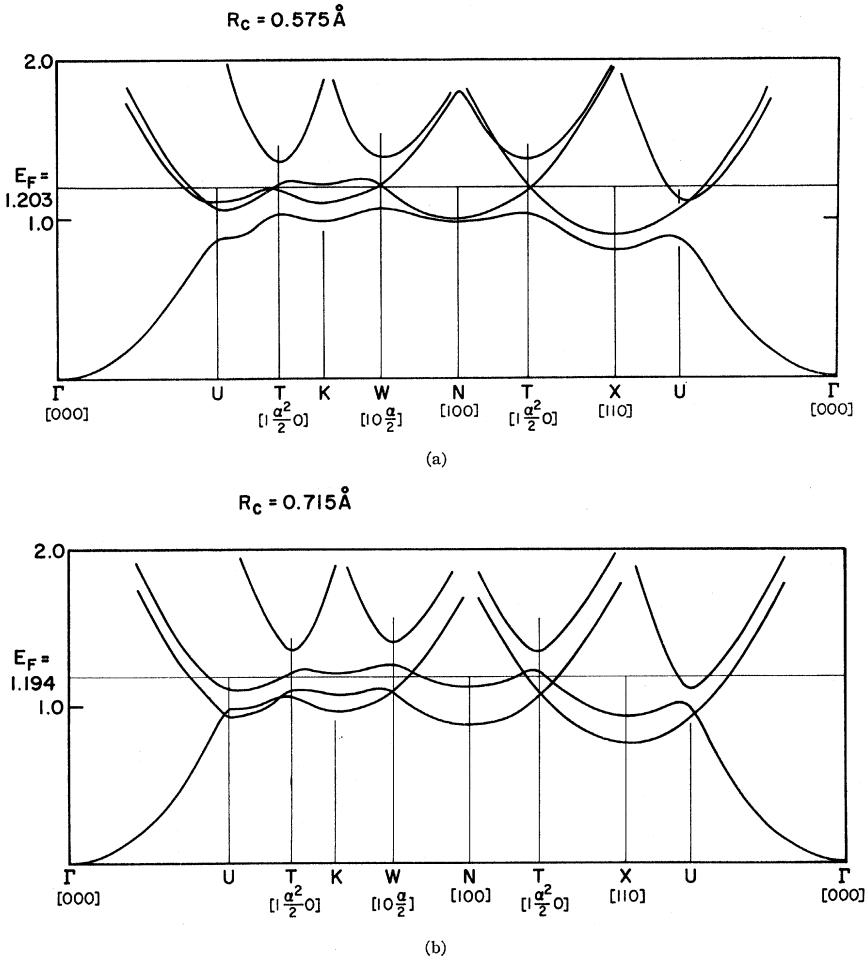

FIG. 12. $E(\mathbf{k})$ versus $\mathbf{k}$ for $\mathbf{k}$ along lines joining points of high symmetry in the zone. The sensitivity of the Fermi-surface structure near points W and T to the values of the band gaps and the Fermi energy is apparent.

The presence of the planes of reflection on the zone (the planes of the square and rhombohedral faces), ensures the existence of lines of band contact[20] (as found previously, for example, in Al). We have solved Eqs. (B1) for the lines of contact and found, for the point T,

$$[y-\tfrac{1}{2}(V_3-V_2)]\left(y-\frac{V_3^2+V_2V_3-2V_1^2}{2V_2}\right)=(\alpha z)^2, \qquad \alpha=c/a \quad (10)$$

in the (100) plane, and

$$[y-\tfrac{1}{2}(V_3-V_2)]\left(y-\frac{V_2^2+V_2V_3-2V_1^2}{2V_2}\right)=x^2 \quad (11)$$

in the (00α) plane, where $\mathbf{K}=(x,y,z)$ is the (wave vector) displacement from T. There are also lines of contact associated with the point W, and their equations are similar to those found for the lines of contact in Al ($\alpha=1$ in what follows), namely,

$$\alpha z[\alpha z-(V_3^2-V_1^2)/(V_3)]=y^2 \quad (12)$$

in the (100) plane, and

$$\alpha z[\alpha z+(V_3^2-V_1^2)/(V_3)]=x^2 \quad (13)$$

in the (010) plane, with $\mathbf{K}=(x,y,z)$ being the displacement from W.

The positions and interpretations of the lines of band contact for both values of R_c are given in Table V, although much can be inferred from the band-structure graphs of Fig. 12. A more complete analysis of the lines of band contact and resulting Fermi-surface structure is deferred to Appendix B, for which the appropriate illustrations are Figs. 10 and 11.

The following structure is *common* to both models: (a) The β-arm ring is connected at eight points to the second-zone hole surface (at its corners); (b) those lines of contact near W which represent degeneracy between the second and third bands lie entirely within the tubes that connect the second-zone hole surface in the extended zone scheme. We repeat that the areas of the connecting tubes are especially sensitive to the choice of Fermi energy because of their small size. For $R_c=0.575$ Å, a 0.4% increase in E_F will, in fact, replace the tubes by tiny pockets of electrons in the third zone.

[20] C. Herring, Phys. Rev. 52, 365 (1937).

TABLE V. A directory of the lines of band contact, giving their intercepts and resulting Fermi-surface structure near W and T. (B4) refers to Eq. (B4), etc.

Symmetry point	Set of lines	Intercepts	Interpretation $R_c=0.575$ Å
T	(B4)(100)	$Y=0.021$	contain the eight points of contact between β arm and second-zone hole sheet
		-1.6[a]	lies entirely within second-zone electron surface in rhombohedral face, first and second bands degenerate
T	(B5)(001)	0.021	lies within β-arm ring, second and third bands degenerate
		-0.19	third and fourth bands degenerate
W	(B7)(100)	$Z=0.0$	second and third bands degenerate,[b] lies within second-zone connecting tubes
		-1.6[a]	first and second bands degenerate
W	(B8)(010)	0.0	same as (B7)
		1.6[a]	
			$R_c=0.715$ Å
T	(B4)(100)	$Y=0.018$	first and second bands degenerate
		0.096	contain the eight points of contact between β-ring and second-zone hole surface
T	(B5)(001)	0.018	first and second bands degenerate
		-0.092	second and third bands degenerate,[b] lies within second-zone connecting tubes
W	(B7)(100)	$Z=0.0$	first and second bands degenerate
		0.114	second and third bands degenerate,[b] lie within second-zone connecting tubes
W	(B8)(010)	0.0	same as (B7)
		-0.114	

[a] Has moved out of symmetry element, hence levels are not degenerate.
[b] Requires third-zone electrons, or tubes that connect the second-zone hole surface.

Each of these pockets will then be connected at four points to corners of the second-zone hole surface. Constant energy surfaces near W are drawn in Fig. 11. The two model pseudopotentials *differ* in the following structure: (c) With $R_c=0.715$ Å, those lines of band contact near T which lie in the (001) plane and connect bands two and three lie entirely within the second-zone connecting tubes. For the $R_c=0.575$ Å alternative, however, neither second-zone connecting tubes nor third-zone electron pockets exist in the rhombohedral face near T. This structure results because one of the two lines of band contact associated with this region represents degeneracy between bands three and four; the other line connects bands one and two. The associated structure is shown in Fig. 10, and compares favorably with measurements of Gantmakher and Krylov[11] on the second-zone hole sheet.

With only the third-zone β arm and second-zone hole surface present, we have computed the density of states directly from evaluating the change in Fermi-surface volume accompanying a small change in Fermi energy. [This procedure leads, of course, to the usual relation, $N(E_F)=(1/4\pi^3)\int_{FS}dS/(|\nabla_k E_k|)$.] We find

$$N(E_F)/N_0(E_F{}^0)=0.91\pm0.01.$$

About 10% of the density of states is lost through the almost complete disappearance of the α arms. The contribution from the second zone is enhanced by about 2% over the free-electron value. The β-arm contribution is reduced by less than 1% of $N_0(E_F{}^0)$,

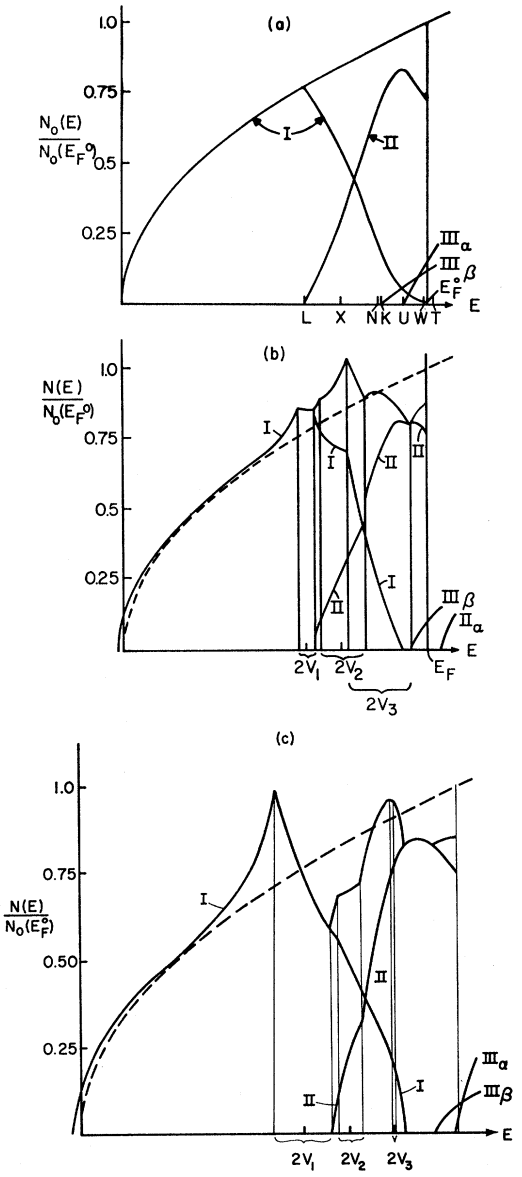

FIG. 13. (a) Contributions to the density of states for the free-electron model in In: I, first zone; II, second zone; III_α, third-zone α-arm system; III_β, third-zone β-arm system. (b) Density of states in the nearly-free-electron model, with $R_c=0.715$ Å as described in the text. The density of states at the Fermi energy corresponds to a band-structure effective mass of 0.85. (c) Density of states with $R_c=0.575$ Å.

because enhancement of $1/|\nabla_k E_k|$ near the neck compensates the substantial loss in area.

A semiquantitative calculation of the density of states at energies below E_F is shown in Figs. 13(a)–13(c). In Fig. 13(a), we have computed the contribution to $N_0(E)/N_0(E_F{}^0)$ from the various zones as a function of E. This follows from

$$N(E)=\frac{1}{4\pi^3}\int_{S(E)}\frac{dS_E}{|\nabla_k E|},$$

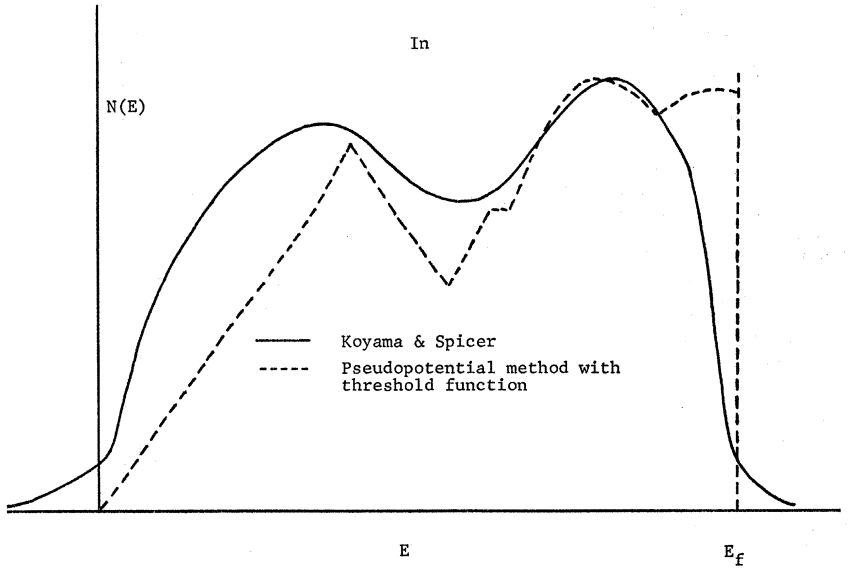

FIG. 14. Photoemission curve superimposed with calculated (scaled) density-of-states curve of Fig. 13(c).

again for the particular case in which $|\nabla_k E| = 2k$ (i.e., the free-electron value). Then

$$N(E)=\left(\frac{1}{8\pi^3 E^{1/2}}\right)[\sum S_i]_E, \qquad (14)$$

where the S_i are the areas of the Fermi surface in the zones i for a Fermi radius $k=E^{1/2}$ (we will confine our attention to zones I, II, and III). In Fig. 13(a), the second-zone (II) surface is shown to contribute for energies $E>E_L$. The third-zone surface contributes when $E>E_U$, and the third-zone α-surface contributes when $E>E_K$.

To account for the effect of the potential and band structure on $N(E)$ [Eq. (14)], we have used the result of Jones[21] derived for the correction to the density of states due to a single zone plane, and have summed these corrections over planes that cut the Fermi surface. The existence of the band gaps now requires the area of the Fermi surface of the first zone, for example, to start diminishing at an energy less than E_L, in fact at E_L-V_1. On the other hand, Fermi-surface area in the second zone first appears at E_L+V_1, as shown in Fig. 13(b) for $R_c=0.715$ Å and Fig. 13(c) for $R_c=0.575$ Å. Similar abrupt changes occur at $E_X\pm V_2$ and $E_N\pm V_3$ as shown, and their magnitudes are also calculated with Eq. (7) of Jones.

The contribution from the first zone terminates in Fig. 13(b), for example, at E_T-V_3 (which is the energy of the first-zone level at W and is the highest first-zone energy). The third-zone contributions commence at the third-zone energies appropriate to K and U as marked in Figs. 13(b) and (c). As mentioned already, the third-zone α system is empty or almost empty at $E=E_F$, also seen in Figs. 13(b) and (c). Contributions from the β system commence below E_F. The result of adding the various terms gives the full curve on Figs. 13(b) and (c), showing general increases in the density of states in the region of the band gaps (as expected) and a few percent decrease around the Fermi energy. Further support for the potential corresponding to $R_c=0.575$ Å is found in the recent photoemission experiments (and their interpretation) by Koyama *et al.*[22] One of the implications of the relatively large band gap V_1 produced by this potential is the appearance of relatively strong structure in $N(E)$ centered about the free-electron energy E_L. This is seen clearly in the measurements reported in Ref. 21 [in which Fig. 13(c) also appears]. The position of the center of the structure relative to the Fermi cutoff gives a rough measure of the energy scale involved; it also gives an order-of-magnitude comparison with the value of η' previously mentioned; i.e.,

$$\frac{V_{000}(E_L)-V_{000}(E_F)}{E_F-E_L}\approx -0.17.$$

Of course there is not necessarily a simple relationship between η and η' (clearly the quantity above depends explicitly only upon η), but we would expect similar orders of magnitude. The experimental and scaled band-structure density-of-states curves are superimposed on each other in Fig. 14.

VI. DISCUSSION

From the band structures of Fig. 12, it is evident that In is essentially as free-electron-like as Al. With the aid of a simple functional form for the effective electron-ion interaction, we have investigated the various topologies possible for the Fermi surface of In, and have succeeded in reproducing the β-arm data with

[21] H. Jones, Proc. Phys. Soc. (London) 49, 250 (1937).

[22] R. Koyama, W. E. Spicer, N. W. Ashcroft, and W. E. Lawrence, Phys. Rev. Letters 19, 1284 (1967).

values of the three principal band gaps shown in Fig. 5. Of the two model form factors we have discussed, the $R_c=0.575$ Å model gives much better agreement near the symmetry point T with the de Haas–van Alphen, cyclotron-mass, and size-effect data. In addition, it matches the caliper dimensions of Gantmakher and Krylov on the principal section of the β arm at U. Finally, the pressure dependence of this third-zone section clearly favors the $R_c=0.575$ Å model. The large positive value of $(d\ln A/dP)$ for the third-zone orbit suggests that V_1 and V_2 are negative. The band gaps, now in eV, are, for $R_c=0.575$ Å: $V_1=-0.66$, $V_2=-0.28$, $V_3=0.037$; and for $R_c=0.715$ Å: $V_1=0.27$, $V_2=0.65$, $V_3=0.90$. It is interesting to record that Golovashkin *et al.*[23] have concluded from optical studies that $|V_1|$ and $|V_2|$ are 0.30 eV and 0.74 eV. These authors ordered the gaps by assuming, as in Al, that $|V_2|>|V_1|$: the agreement with the $R_c=0.575$ Å model is remarkably good if we make the opposite assumption.

As to the question of the presence of α arms, if they exist, they must be very small. Their principal areas [lying in (011) planes] would probably be no larger than 1/20 of the principal area of the β arm.

There is little experimental evidence favoring the second-zone connecting tubes. In the earlier work of Brandt and Rayne,[24] two sets of low-frequency oscillations are observed. One, as we have said, is unmistakably identified with the β-arm neck. The other has a symmetry that is consistent with the second-zone connecting tubes as given by $R_c=0.575$ Å; here the tubes actually intersect at the symmetry point W, to give areal minima in the (110) planes. The frequencies of the latter set of oscillations also agree in magnitude with those of the $R_c=0.575$-Å model. A comparison is shown in Fig. 11.

One consequence of the connecting regions between the second-zone sheets is the possibility of extended, or even open, orbits for fields accurately aligned along [100] or [010] directions (see Figs. 8 and 9). The effect of these orbits on galvanomagnetic properties is difficult to assess but, for example, there may be a small nonsaturating component in the transverse magnetoresistance at high fields for strain-free single crystals. The present measurements of transverse magnetoresistance due to Gaidukov[25] use fields of up to 24 kG and there is evidently no large nonsaturating component. (Since the connecting regions are so small, the condition on alignment is rather severe.)

There is little other experimental evidence supporting the existence of the second-zone tubes. Oblique sections of these regions do permit caliper dimensions of a substantial size, and it is possible that they are responsible for the "y" oscillations of Gantmakher and Krylov in their size-effect measurements. These authors remark that the "y" oscillations give a range of dimensions whose maxima are considerably in excess of those expected on the α (and β) systems and are otherwise difficult to relate to a closed second-zone sheet. We have also found (see Figs. 8–12) regions on the connecting tubes with small Gaussian curvature, and regions where the Gaussian curvature R changes sign (saddle points). The effect of these parts of the Fermi surface will be to increase integrals weighted by R^{-1} appearing in the expression for the attenuation parameter over the free-electron value. This is in qualitative agreement with the observation of Bliss and Rayne[26] of attenuations in excess of the free-electron values for certain crystal directions.

We have used the form factor given in Eq. (2) with $R_c=0.715$ Å and 0.575 Å, respectively, to compute the resistivity ρ of liquid In just above the melting point. According to Ziman[27] the lowest-order expression for ρ_L is given by

$$\rho_L=\frac{4\pi^3\hbar}{e^2k_F}Z\int_0^1 V^2(x)a(x)x^3dx, \tag{15}$$

where, again, x is the wave-number variable, measured in units of $2k_F$. The function $a(x)$ appearing in (15) is the static structure factor for the ions in liquid In. We have calculated ρ using the experimental $a(x)$ of Ocken and Wagner[28] and the model hard-sphere function of Ashcroft and Lekner,[29] the two curves being quite similar. The results are, respectively, 38 $\mu\Omega$ cm and 41 $\mu\Omega$ cm for $R_c=0.715$ Å, and 34 $\mu\Omega$ cm and 36 $\mu\Omega$ cm for $R_c=0.575$ Å. These figures are to be compared with the experimental value of 33 $\mu\Omega$ cm at the melting temperature $T_M=156$°C. Both values of R_c, therefore, yield values for ρ_L that are within the probable limitations of (15), and hence the two possibilities for the potential cannot be distinguished between by appealing to the resistivity of liquid In. Nor is the form of the ion-ion interaction a *decisive* test—we have calculated the pair potential $\phi(\rho)$ (where $\rho=2k_Fr$) for two ions separated by a distance r by the methods outlined in Ashcroft and Langreth.[30] Using their Eq. (7), the potential ϕ [in units of $(\frac{2}{3})E_F$] for the two values of R_c is shown in Fig. 15. Both curves are in reasonable agreement with the hard-core dimension resulting from an analysis of the structure-factor data in terms of the Percus-Yevick equation (see Ref. 27). In the units of Fig. 15, the hard-sphere diameter is $\rho_{HS}=8.40$; measuring $(\frac{3}{2})kT_M$ from the principal minima of the potential

[23] A. I. Golovashkin *et al.*, Zh. Eksperim. i Teor. Fiz. **51**, 1622 (1966) [English transl.: Soviet Phys.—JETP **24**, 1093 (1967)].
[24] See Fig. 7 of the second paper of Ref. 9 (also shown in our Fig. 11).
[25] Yu. P. Gaidukov, Zh. Eksperim. i Teor. Fiz. **49**, 1049 (1965) [English transl.: Soviet Phys.—JETP **22**, 730 (1966)].
[26] E. S. Bliss and J. A. Rayne, Phys. Letters **23**, 38 (1966).
[27] J. M. Ziman, Phil. Mag. **6**, 1013 (1961).
[28] H. Ocken and C. N. J. Wagner, Phys. Rev. **149**, 767 (1966).
[29] N. W. Ashcroft and J. Lekner, Phys. Rev. **145**, 83 (1966). We use a packing fraction of 0.456 appropriate to the melting temperature.
[30] N. W. Ashcroft and D. C. Langreth, Phys. Rev. **159**, 500 (1967).

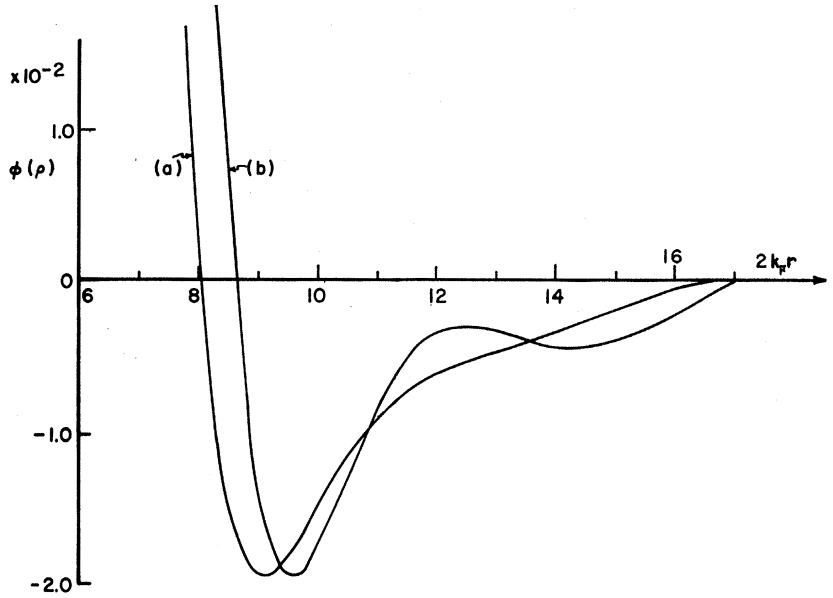

FIG. 15. Ion-ion interactions calculated from Eq. (7) of Ref. 28 for an electron density appropriate to liquid In just above its melting point. (a) $R_c=0.575$ Å, (b) $R_c=0.715$ Å. Note that $\rho=2k_Fr$ and energies are in units of $(\frac{2}{3})E_F$.

curves (see Ref. 18) give intercepts $\rho=8.1$ and $\rho=8.6$ for $R_c=0.575$ and 0.715 Å, respectively, both values bracketing the hard-sphere value.

In summary, the form factor (2) with $R_c=0.575$ Å gives reasonable agreement with the established galvanomagnetic data and is also in accord with effective-mass data, both cyclotron resonance and specific heat. There may, of course, be small corrections to (2) arising from the l-dependent nature of the pseudopotential and truncation of the secular equation. Most of these are assumed to be absorbed in the parametrization (i.e., in R_c) and the over-all agreement suggests that they are small. Finally, we note that there may be some small[31] additional anisotropy in the Fermi surface resulting from spin-orbit coupling. These effects have been neglected in the present treatment in which the Kramers degeneracy is unresolved.

ACKNOWLEDGMENTS

We are grateful to Professor J. W. Wilkins for many useful and stimulating discussions throughout the course of this work. We wish to thank Professor R. G. Chambers, Professor J. A. Rayne, and Dr. A. S. Joseph for helpful comments.

APPENDIX A

The level structure at the four symmetry points of interest is determined by the following secular equations:

$$\text{At } K, \quad \begin{vmatrix} T_K & V_1 & V_1 \\ V_1 & T_K & V_3 \\ V_1 & V_3 & T_K \end{vmatrix} = 0, \tag{A1}$$

$$\text{at } U, \quad \begin{vmatrix} T_U & V_1 & V_1 \\ V_1 & T_U & V_2 \\ V_1 & V_2 & T_U \end{vmatrix} = 0, \tag{A2}$$

$$\text{at } W, \quad \begin{vmatrix} T_W & V_3 & V_1 & V_1 \\ V_3 & T_W & V_1 & V_1 \\ V_1 & V_1 & T_W & V_3 \\ V_1 & V_1 & V_3 & T_W \end{vmatrix} = 0, \tag{A3}$$

$$\text{and at } T, \quad \begin{vmatrix} T_T & V_2 & V_1 & V_1 \\ V_2 & T_T & V_1 & V_1 \\ V_1 & V_1 & T_T & V_3 \\ V_1 & V_1 & V_3 & T_T \end{vmatrix} = 0, \tag{A4}$$

where, for example, $T_U=k_U^2-E$. The solutions to these give the following levels:

$$\text{At } K, \quad E=k_K^2-V_3, \quad E_\pm=k_K^2+\tfrac{1}{2}V_3\pm[(\tfrac{1}{2}V_3)^2+2V_1^2]^{1/2}, \tag{A5}$$

$$\text{at } U, \quad E=k_U^2-V_2, \quad E_\pm=k_U^2+\tfrac{1}{2}V_2\pm[\tfrac{1}{2}(V_2)^2+2V_1^2]^{1/2}, \tag{A6}$$

$$\text{at } W, \quad E=k_W^2-V_3 \text{ (doubly degenerate)}, \quad E_\pm=k_W^2+V_3\pm 2V_1, \tag{A7}$$

$$\text{and at } T, \quad E_1=k_T^2-V_3, \quad E_2=k_T^2-V_2, \quad E_\pm=k_T^2+\tfrac{1}{2}(V_3+V_2)\pm[(\tfrac{1}{2}(V_3-V_2))^2+(2V_1)^2]^{1/2}. \tag{A8}$$

As in paper I, we now set $E=E_F$, and express V_2 or V_3 as a function of V_1 for each level. These curves [represented by (A9)–(A12)] separate regions in which different numbers of zones (indicated in Figs. 2–5) are occupied at the given symmetry point. Letting

[31] The spin-orbit coupling parameter has a value on the order of 0.5 eV in lead (Ref. 5). In indium, we expect the parameter to be $\gtrsim(49/82)^5\times 0.5$ eV ≈ 0.04 eV.

$\Delta_K=E_F-k_K^2$, and so on, we find at K,

$$V_3=-\Delta_K,\qquad V_3=\Delta_K-(2/\Delta_K)V_1^2, \tag{A9}$$

and at U,

$$V_2=-\Delta_U,\qquad V_2=\Delta_U-(2/\Delta_U)V_1^2. \tag{A10}$$

Now all three band gaps determine the levels at T and we use the constraint, $V_3=V_2+0.04$, consistent with a large range of R_c, to obtain

$$V_2=-\Delta_T,\quad V_2=-\Delta_T-0.04,\quad V_2=\Delta_T-0.02\pm[(0.02)^2+4V_1^2]^{1/2}. \tag{A11}$$

Similarly, at W the lines separating zones of occupancy are $V_3=-\Delta_W$ (corresponding to the doubly degenerate state) and

$$V_3=-\Delta_W\pm 2V_1. \tag{A12}$$

We must apply a small correction to E_F and thus also to the Δ's as a result of the presence of band gaps. The second-order perturbation-theory result used in I gives

$$E_F=E_F^0-(1.30V_1^2+0.43V_2^2+1.16V_3^2) \tag{A13}$$

if we bring in only those Bragg planes that cut the Fermi surface. The use of (A13) rather than E_F^0 modifies the curves only slightly (A11) and (A12).

APPENDIX B

To discuss the topological structure of the Fermi surface in the vicinity of W and T, we reduce the 4×4 determinants discussed in Appendix A to a more convenient form. We can rewrite (A3) and (A4) in cases where the diagonal elements are not equal as

$$\begin{vmatrix} T_1 & V_3 & V_1 & V_1 \\ V_3 & T_2 & V_1 & V_1 \\ V_1 & V_1 & T_3 & V_2 \\ V_1 & V_1 & V_2 & T_4 \end{vmatrix} = (T_1T_2-V_3^2)(T_3T_4-V_2^2)-V_1^2(T_1+T_2-2V_3)(T_3+T_4-2V_2)=0. \tag{B1}$$

Let us consider first the point T. We parametrize the kinetic energy in terms of wave-vector displacements $\mathbf{K}=(x,y,z)$ from the point T (with x parallel to [100], etc.):

$$T_1=\gamma+2x+2d_1y,\quad T_2=\gamma-2x+2d_1y,\quad T_3=\gamma+2\alpha z-2d_2y,\quad T_4=\gamma-2\alpha z-2d_2y, \tag{B2}$$

where $\gamma=|\mathbf{K}|^2-\Delta$, $\Delta=E_F-E_T$,

$d_1=(NT)$,

$d_2=(XT)$.

Equation (B1) now becomes

$$[(\gamma+2d_1y)^2-(2x)^2-V_3^2][(\gamma-2d_2y)^2-(2\alpha z)^2-V_2^2]-4V_1^2(\gamma+2d_1y-V_3)(\gamma-2d_2y-V_2)=0. \tag{B3}$$

This nicely displays the reflection symmetry in the (100) and (001) planes at T, and factorizes for $x=0$ or $z=0$ to give lines of band contact in these planes.

(i) In the (100) plane, $(\gamma+2d_1y-V_3)$ is a factor of (B3). Substitution of $\gamma=V_3-2d_1y$ into the other factor yields the lines of double roots:

$$[y-\tfrac{1}{2}(V_3-V_2)]\times[y+(V_3^2+V_2V_3-2V_1^2)/2V_3]=(\alpha z)^2, \tag{B4}$$

which intersect the β ring at the eight points of contact with the second-zone hole surface (in fact at its corners). Notice that, for V_3 small (as in the case for $R_c=0.575$ Å), there is only one solution that lies within the symmetry element. The other solution approaches a straight line as $V_3\to0$, and strongly affects the structure of the β-arm neck (as shown in Fig. 11).

(ii) We similarly obtain, for the (001) plane,

$$[y-\tfrac{1}{2}(V_3-V_2)]\times[y-(V_2^2+V_2V_3-2V_1^2)/2V_2]=x^2, \tag{B5}$$

giving lines which lie inside the hole-surface connecting tubes for $R_c=0.715$ Å (see Table IV for comments).

For each model pseudopotential, we find the (100) and (001) sections of the Fermi surface by solving (B1) on the machine. These are shown in Figs. 10 and 11 with lines of contact drawn in.

The structure at W is given by (B1) if we replace V_2 by V_3 and parametrize kinetic energies in terms of wave-vector displacements $\mathbf{K}=(x,y,z)$ from W as follows:

$$T_1=\gamma+2x+\alpha z,\quad T_2=\gamma-2x+\alpha z,\quad T_3=\gamma+2x-\alpha z,\quad T_4=\gamma-2x-\alpha z, \tag{B6}$$

where $\gamma=x^2+y^2+z^2-\Delta$ and $\Delta=E_F-E_W$. Because of the higher symmetry at W, one set of contact lines is obtained from the other by a reflection through $z=0$ and a rotation through $\frac{1}{2}\pi$ about the z axis (as in aluminum). In the (100) plane the contact line is

$$\alpha z[\alpha z-(V_3^2-V_1^2)/V_3]=y^2, \tag{B7}$$

and in the (010) plane

$$\alpha z[\alpha z+(V_3^2-V_1^2)/V_3]=x^2. \tag{B8}$$

For both $R_c=0.575$ Å and $R_c=0.715$ Å, the sets of lines

at W which represent degenerate second and third levels lie within the second-zone hole surface. In general, when such a situation exists on the rhombohedral or square faces of the zone, we must have either the third zone occupied or tubes that connect the second-zone hole surface in the extended zone scheme.

APPENDIX C

The electron-phonon enhancement factor for a (Bloch) state $|\mathbf{k},n\rangle$ of wave vector $\mathbf{k}$ in the nth band is given in second-order perturbation theory by

$$\lambda_{\mathbf{k}}{}^{(n)}=\frac{1}{S}\int_{FS}\frac{dS_{\mathbf{p}}}{4\pi}\sum_{\lambda}\frac{|g_{\mathbf{k}}{}^{(n)}{}_{-\mathbf{p},\lambda}|^2}{\omega_{\mathbf{k}-\mathbf{p},\lambda}},$$

and the enhancement factor for an orbit Γ is

$$\lambda_{\Gamma}=\frac{1}{l_{\Gamma}}\oint_{\Gamma}dk_{\Gamma}\lambda_{\mathbf{k}}{}^{(n)}.$$

Since most of the Fermi surface in In is free-electron-like, we let $|\mathbf{p}\rangle$ be a single plane wave. For most points on large second-zone orbits, $|\mathbf{k},2\rangle$ is also very nearly a single plane wave, but for most points on any third-zone orbit this is not the case, and we must write, e.g.,

$$\langle\mathbf{r}|\mathbf{k},3\rangle=c_1e^{i\mathbf{k}\cdot\mathbf{r}}+c_2e^{i(\mathbf{k}-[1,1,\alpha])\cdot\mathbf{r}}+c_3e^{i(\mathbf{k}-[1,1,\bar{\alpha}])\cdot\mathbf{r}}.$$

Hence, for the second zone, we may write

$$\omega_{\mathbf{q}\lambda}(g_{\mathbf{q}}{}^{(2)})^2=(\boldsymbol{\varepsilon}_{\mathbf{q}\lambda}\cdot\mathbf{q}V_{\mathbf{q}})^2,$$

where $\boldsymbol{\varepsilon}_{\mathbf{q}\lambda}$ is the polarization vector for a phonon of polarization λ and frequency $\omega_{\mathbf{q}\lambda}$. Both quantities are understood to be periodically extended beyond the first zone. However, the analogous expression for the third-zone state above is

$$\omega_{\mathbf{q}\lambda}|g_{\mathbf{q}.\lambda}{}^{(3)}|^2=|c_1\boldsymbol{\varepsilon}_{\mathbf{q}\lambda}\cdot\mathbf{q}V_{\mathbf{q}}+c_2\boldsymbol{\varepsilon}_{\mathbf{q}\lambda}\cdot(\mathbf{q}-[1,1,\alpha])V_{\mathbf{q}-[1,1,\alpha]}+c_3\boldsymbol{\varepsilon}_{\mathbf{q}\lambda}\cdot(\mathbf{q}-[1,1,\bar{\alpha}])V_{\mathbf{q}-[1,1,\bar{\alpha}]}|^2.$$

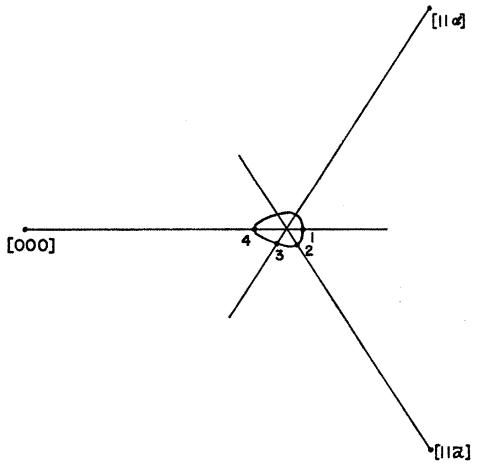

FIG. 16. Points on the principal orbit of the β arm for which we have tabulated the mixing coefficients.

TABLE VI. Mixing coefficients for third zone (see text and Fig. 16).

Point	c_1	c_2	c_3
1	−0.90	0.30	0.30
2	−0.74	0.66	−0.13
3	−0.33	0.94	−0.02
4	0.0	0.71	−0.71

Now if $\mathbf{k}$ is on the (third zone) Fermi surface, $\mathbf{k}-(1,1,\alpha)$ and $\mathbf{k}-(1,1,\bar{\alpha})$ are very close to the Fermi surface, and to a good approximation the integrals arising from the three direct terms are equal, so that since

$$\sum_{i=1}^{3}c_i{}^2=1,$$

the sum of direct terms gives a result equal to that for the second zone. As a result, the difference between the enhancement factor for some third-zone orbit, Γ, and a typical second-zone orbit is

$$\Delta_{\Gamma}=\lambda_{\Gamma}{}^{(3)}-\lambda^{(2)}=\frac{1}{l_{\Gamma}}\oint_{\Gamma}dl_{\Gamma}\sum_{i\neq j}c_ic_jI_{ij},$$

where

$$I_{ij}=\frac{1}{S}\int\frac{dS}{4\pi}\times\sum_{\lambda}\frac{[\boldsymbol{\varepsilon}_{\mathbf{q}\lambda}\cdot(\mathbf{q}+\mathbf{G}_i)][\boldsymbol{\varepsilon}_{\mathbf{q}\lambda}\cdot(\mathbf{q}+\mathbf{G}_j)]V_{(\mathbf{q}+\mathbf{G}i)}V_{(\mathbf{q}+\mathbf{G}j)}}{\omega_{\mathbf{q}\lambda}{}^2},$$

$$G_1=0,\quad G_2=(1,1,\alpha),\text{ and }G_3=(1,1,\bar{\alpha}).$$

We have performed a rough calculation of Δ for the principal orbit of the β arm, since Δ will probably be larger for most of the other orbits on the β arm.

We break the third-zone orbit up into three segments (see Fig. 16), within each of which one of the c_i's is small, so that within each of the segments we have only to evaluate a single integral. We tabulate, below, the mixing coefficients for representative points on the third-zone orbit, and contrast these with typical ratios of the two largest mixing coefficients on the second zone. The second-zone figures were obtained by averaging over each of the three types of zone faces, approximating the actual segment of surface by a spherical cap. (See Tables VI and VII.)

TABLE VII. Ratios of two largest second-zone mixing coefficients (see text).

Zone plane, G	c_1/c_2
$[11\alpha]$	8
[200]	13
$[002\alpha]$	20

We assume the I_{ij} to be uniform over a given segment, and perform the orbit average by averaging the products $c_ic_jI_{ij}$, with c_ic_j averaged over the given segment. The geometry involved is quite complex and only very rough numerical estimates of the integrals I_{ij} have been made, from which we conclude that

$$0.10<(\lambda^{(3)}-\lambda^{(2)})/\lambda^{(2)}<0.20.$$

The processes that contribute to these I_{ij} can be classified as, say, N (only longitudinal phonons involved) and U (both longitudinal and transverse phonons involved). Roughly $\frac{2}{3}$ of the above factor results from N processes, partly because there is some cancellation between contributions from U processes.

APPENDIX D

To calculate the pressure dependence of de Haas–van Alphen areas, we use the formula

$$\frac{d\ln A}{dP}=\frac{\partial\ln A}{\partial\ln n}\frac{d\ln n}{dP}+\frac{\partial\ln A}{\partial\ln\alpha}\frac{d\ln\alpha}{dP}+\sum_{G=1}^{3}\left(\frac{\partial\ln A}{\partial V_G}+\frac{\partial\ln A}{\partial\ln E_F}\frac{\partial\ln E_F}{\partial V_G}\bigg|_{\text{Vol}}\right)\frac{dV_G}{dP}.$$

The first two terms account for the changes in electron density n and ratio of lattice constants α. The last term accounts for the change in band gaps; $\partial\ln E_F/\partial\ln V_G|_{\text{Vol}}$ is the shift in Fermi energy, which accompanies a change in V_G in such a way that the Fermi surface encloses constant volume. The V_G's change according to (2), and we shall take into account possible changes in the parameter R_c with energy.

For the principal section of the β arm, we find that $d\ln A/dP=[4.41+5.10\eta]K_T$, where K_T is the compressibility and $\eta=d\ln R_c/d\ln E$. The various contributions are (in units of K_T): 0.67 from the electron density, 1.21 from the lattice constants,[18] and $2.25+3.94\eta$ from the band gaps. Comparing this with the result of Anderson, O'Sullivan, and Schirber, $d\ln A/dP=(3.4\pm0.15)K_T$, we would deduce that $\eta=-0.18$. We note however that uncertainty in this value for η is greater by a factor of four than experimental uncertainty in $d\ln A/dP$. Finally, we point out again that our calculations of $d\ln A/dP$ for second-zone orbits give numbers about 20% smaller than the experimental ones, as do the calculations of Anderson, O'Sullivan, and Schirber.

PHYSICAL REVIEW VOLUME 175, NUMBER 3 15 NOVEMBER 1968

Third-Order Elastic Constants of Aluminum*†

J. F. Thomas, Jr.‡
Department of Physics and Materials Research Laboratory, University of Illinois, Urbana, Illinois 61801
(Received 5 April 1968)

The complete set of six third-order elastic constants of single-crystal Al has been experimentally determined by measuring both hydrostatic-pressure and uniaxial-stress derivatives of the natural sound velocities using a two-specimen interferometric technique. The specimens were neutron-irradiated to eliminate dislocation effects from the uniaxial experiments. A self-consistent set of hydrostatic-pressure derivatives of the second-order elastic constants has been calculated from the measured third-order constants. The third-order elastic constants have also been used to calculate the thermal expansion in the anisotropic-continuum model at both high and low temperatures, and a comparison has been made with the directly measured expansion coefficients.

INTRODUCTION

HIGHER-ORDER elastic constants provide an efficient measure of many aspects of lattice anharmonicity. In particular, the third-order elastic constants are useful in the calculation of many mechanical and thermal properties related to the anharmonic nature of the lattice potential energy. In addition, the third-order elastic constants would be expected to provide useful new information on the nature of cohesive properties and interatomic forces.

The most powerful method for obtaining third-order elastic constants is the measurement of sound-velocity changes with applied homogeneous stress. Basic measurements of this type utilize simple modifications of the well-known megacycle pulse-echo technique. Early measurements were restricted to velocity change with applied hydrostatic pressure. For a cubic crystal, this gives three experimental numbers which are related to five of the six third-order elastic constants. To obtain sufficient information to measure all six third-order elastic constants, it is necessary to utilize a deviatoric stress such as uniaxial compression.

* This research was supported by the U. S. Atomic Energy Commission under Contract No. AT(11-1)-1198.
† Based on a thesis submitted in partial fulfillment of the requirements for the degree of Doctor of Philosophy at the University of Illinois, 1968.
‡ Present address: Department of Physics, University of Virginia, Charlottesville, Va. 22903.